Published in final edited form as:

IEEE Trans Biomed Eng. 2015 April ; 62(4): 1108–1119. doi:10.1109/TBME.2014.2369491.

Anatomy-Guided Dense Individualized and Common Connectivity-Based Cortical Landmarks (A-DICCCOL)

Xi Jiang [Student Member, IEEE],
Cortical Architecture Imaging and Discovery Lab, Department of Computer Science and Bioimaging Research Center, The University of Georgia, Athens, GA 30602 USA

Tuo Zhang,
School of Automation, Northwestern Polytechnical University, Xi'an 710072, China

Cortical Architecture Imaging and Discovery Lab, Department of Computer Science and Bioimaging Research Center, The University of Georgia, Athens, GA 30602 USA

Dajiang Zhu,
Cortical Architecture Imaging and Discovery Lab, Department of Computer Science and Bioimaging Research Center, The University of Georgia, Athens, GA 30602 USA

Kaiming Li,
School of Automation, Northwestern Polytechnical University, Xi'an 710072 China

Cortical Architecture Imaging and Discovery Lab, Department of Computer Science and Bioimaging Research Center, The University of Georgia, Athens, GA 30602 USA

Hanbo Chen,
Cortical Architecture Imaging and Discovery Lab, Department of Computer Science and Bioimaging Research Center, The University of Georgia, Athens, GA 30602 USA

Jinglei Lv,
School of Automation, Northwestern Polytechnical University, Xi'an 710072 China

Cortical Architecture Imaging and Discovery Lab, Department of Computer Science and Bioimaging Research Center, The University of Georgia, Athens, GA 30602 USA

Xintao Hu,
School of Automation, Northwestern Polytechnical University, Xi'an 710072 China

Junwei Han,
School of Automation, Northwestern Polytechnical University, Xi'an 710072 China

Dinggang Shen,
Department of Radiology, University of North Carolina, Chapel Hill, NC 27599 USA

*T. Liu is with the Cortical Architecture Imaging and Discovery Lab, Department of Computer Science and Bioimaging Research Center, The University of Georgia, Athens, GA 30602 USA (tliu@cs.uga.edu).

This paper has supplementary downloadable material available at http://ieeexplore.ieee.org. (File size: 1 MB).

Color versions of one or more of the figures in this paper are available online at http://ieeexplore.ieee.org.

Authors' photographs and biographies not available at the time of publication.

Lei Guo, and
School of Automation, Northwestern Polytechnical University, Xi'an 710072 China

Tianming Liu* **[Senior Member, IEEE]**

Abstract

Establishment of structural and functional correspondences of human brain that can be quantitatively encoded and reproduced across different subjects and populations is one of the key issues in brain mapping. As an attempt to address this challenge, our recently developed Dense Individualized and Common Connectivity-based Cortical Landmarks (DICCCOL) system reported 358 connectional landmarks, each of which possesses consistent DTI-derived white matter fiber connection pattern that is reproducible in over 240 healthy brains. However, the DICCCOL system can be substantially improved by integrating anatomical and morphological information during landmark initialization and optimization procedures. In this paper, we present a novel anatomy-guided landmark discovery framework that defines and optimizes landmarks via integrating rich anatomical, morphological, and fiber connectional information for landmark initialization, group-wise optimization and prediction, which are formulated and solved as an energy minimization problem. The framework finally determined 555 consistent connectional landmarks. Validation studies demonstrated that the 555 landmarks are reproducible, predictable, and exhibited reasonably accurate anatomical, connectional, and functional correspondences across individuals and populations and thus are named anatomy-guided DICCCOL or A-DICCCOL. This A-DICCCOL system represents common cortical architectures with anatomical, connectional, and functional correspondences across different subjects and would potentially provide opportunities for various applications in brain science.

Index Terms

Anatomy; cortical landmarks; DTI; fMRI; structural connectivity

I. INTRODUCTION

Establishment of structural and functional correspondences of human brain across different subjects and populations is one of the important issues in the brain mapping field. For several decades, three major categories of approaches have been largely adopted in the brain mapping field to establish the correspondences of brain regions across individuals, and remarkable successes have been achieved by those approaches. The first category is brain image registration algorithms (e.g., [1]–[9]). In general, brain image registration methods are mainly concerned with morphological correspondences across individuals. The second category is cortical parcellations (e.g., [10]–[13]). These cortical parcellation approaches typically designed certain criteria to define cortical region boundaries with the aim of establishing correspondences during parcellation of multiple brains. The third category is manual/semiautomatic regions of interests (ROI) analysis (e.g., [14]–[16]). The ROI-based correspondence establishment methods are usually suitable for specific application scenarios.

Alternatively, several recent studies attempted to define and discover consistent and common brain cortical landmarks with intrinsic structural and functional correspondences across different subjects and populations [16]–[21]. In particular, several multimodal DTI/fMRI studies [16]–[24] have demonstrated the close relationships between DTI-derived fiber connection patterns and brain functions. This provides direct supporting evidence to the connectional fingerprint concept [25], which premises that each brain's cytoarchitectonic area has a unique set of extrinsic inputs and outputs that largely determines the functions that each brain area performs. Based on these principles, we developed and validated a data-driven connectional landmark discovery approach dubbed as: Dense Individualized and Common Connectivity-based Cortical Landmarks (DICCCOL) in [21], which identified 358 consistent connectional landmarks. The basic idea was to optimize the localizations of each initial DICCCOL landmark in individual brains by maximizing the group-wise consistency of their DTI-derived white matter fiber connectivity patterns [21]. Our validation studies have demonstrated that the DICCCOLs provide reasonably good intrinsically established correspondences across subjects and populations, and these 358 DICCCOLs have been released online at http://dicccol.cs.uga.edu.

However, the DICCCOL system reported in [21] merely considers the DTI-derived fiber connectivity pattern consistency across different subjects as the metric during landmark identification and can be substantially improved by integrating additional meaningful anatomical, morphological, and fiber connectional information during the landmark identification. Moreover, the landmark initialization for the DICCCOL was merely based on randomly sampled grid points in a template brain. Each grid of initialized landmarks in the template brain was then registered to other brains via linear registration, and the landmark optimization was performed afterward [21]. However, anatomical interindividual variability sometimes misleads the process of normalization. For example, in some brains, the central fissure stops higher than the usual and misleads the registration of the pre- and postcentral gyri. As a consequence, the same corresponding landmark might be misplaced in certain brains. This scenario is illustrated in Fig. 1 as an example. Here, we initialized a corresponding landmark located on the left precentral gyrus (shown as yellow bubble) in three example brains from the template brain via linear registration. It is apparent that the landmark initializations for the first two brains were reasonably accurate (roughly located on the left precentral gyrus), but the initialization for the third brain was wrong (located on the left postcentral gyrus). Therefore, the following landmark optimization procedure would have difficulty in finding consistent fiber connection patterns for these inconsistently initialized landmarks due to image registration error caused by anatomical interindividual variability and would potentially miss this possibly consistent landmark.

In this paper, we substantially improved the identification framework of our original DICCCOL system in [21] and introduced the anatomy-guided DICCCOL or A-DICCCOL. Our major improvements are: first, instead of randomly sampled grid points in a template brain as the initialized landmarks in original DICCCOL system [21], we initialized the connectional landmarks on corresponding gyri/sulci under anatomical guidance for each brain to improve the accuracy of landmark initialization and thus facilitate the landmark optimization and discovery procedure. Second, instead of merely considering the DTI-derived fiber connection pattern similarity as the metric in the previous DICCCOL system,

we added meaningful anatomical, structural connection pattern homogeneity, and spatial information during the group-wise landmark optimization procedure. Specifically, in this paper, three new constraints including anatomical, structural connection pattern homogeneity, and spatial constraints, as well as the previous adopted structural connection pattern similarity constraint, were jointly modeled and integrated together to optimize the landmark locations within individual brains. Extensive experiments have demonstrated the effectiveness and meaningfulness of those newly added constraints in seeking group-wise consistent and corresponding connectional landmarks in individual brains. Third, we applied the proposed connectional landmark discovery procedures on higher angular resolution diffusion imaging (HARDI) data and recently publicly released Human Connectome Project (HCP) high-quality DTI data (Q1 release) [26], and via different fiber tracking software tools to examine the consistency of the DTI-derived connectional landmarks, which is another validation improvement than the previous DICCCOL system. Our proposed framework finally identified 555 new and consistent connectional landmarks, called the anatomy-guided DICCCOL or A-DICCCOL here. Extensive validations based on DTI, HARDI, and fMRI datasets have demonstrated that the 555 landmarks are reproducible, predictable, and exhibit reasonably accurate anatomical, connectional, and functional correspondences across individuals and populations.

II. DATA ACQUISITION AND PREPROCESSING

In this paper, we used five different multimodal DTI/HARDI/fMRI datasets for initialization, optimization, determination, prediction, and validation of A-DICCCOL landmarks, as summarized in Table I. In particular, we randomly selected ten subjects with DTI data from Dataset #1 as the model brains (see Fig. 2) for landmark initialization and the following group-wise optimization and identification. The remaining subjects from Datasets #1–#5 were used as the testing brains (see Fig. 2). In brief, Dataset #1 included 23 healthy adult students recruited under IRB approval. Working memory [27] task-based fMRI (T-fMRI) and DTI scans were acquired for these participants at the University of Georgia (UGA) Bioimaging Research Center (BIRC) under IRB approval. Dataset #2 included the DTI and five T-fMRI scans of 13 healthy young adults recruited at UGA BIRC under IRB approval. The scans were performed on a GE 3T Signa MRI system using an eight-channel head coil at the UGA BIRC. The five T-fMRI scans were based on in-house verified paradigms including emotion [28], empathy [29], fear [29], semantic decision making [30], and working memory [27] tasks, which were also detailed in [21]. Dataset #3 included 20 elderly healthy subjects recruited and scanned at the UGA BIRC under IRB approval. DTI dataset was acquired using the same imaging parameters as those in Datasets #1 and #2. Dataset #4 included 68 subjects from recently publicly released large-scale HCP high-quality DTI data (Q1 release) [26]. Dataset #5 included full-brain coverage HARDI images acquired from five adult subjects using a Siemens 3T Trio MR Scanner at UNC Chapel Hill [31]. The details of acquisition parameters and pre-processing steps of the five datasets are referred to supplemental materials and [32], [33].

III. A-DICCCOL IDENTIFICATION

Fig. 2 summarizes the flowchart of the computational framework for the A-DICCCOL identification. In total, there are four major steps as shown by the numbers: landmark initialization, landmark optimization, landmark determination, and landmark prediction. Details will be covered in the subsequent sections.

A. Landmark Initialization

As mentioned in Section I and detailed in [21], the landmark initialization for our previous DICCCOL system was only based on randomly sampled grid points (2056) in a template brain. Then, each grid of initialized landmarks in the template brain was registered to other subjects using the linear registration algorithm FSL FLIRT [35], and landmark optimization was performed afterward [21]. However, the accuracy of landmark initialization across different subjects might be affected due to the anatomical interindividual variability, and thus, the landmark optimization procedure might be hampered. In this A-DICCCOL discovery framework, we refined the landmark initialization procedure by initializing corresponding landmark on the same gyrus/sulcus under anatomical guidance across different subjects to improve the accuracy of landmark initialization and thus to facilitate the landmark optimization and discovery procedure.

Specifically, first, as mentioned in Section II, ten subjects were randomly selected from Dataset #1 as the group of model brains (see Fig. 2) for landmark initialization and the following group-wise optimization and determination. It is noted that we randomly selected one of the ten model brains as the template, and other model brains were linearly registered to it so that their global shape differences were removed, and their cortical surfaces were in the same space for comparison and landmark initialization. Second, for each model brain, the roughly anatomically corresponding landmarks on the cortical surfaces were interactively labeled by two experts and further checked by the third expert according to the brain template used in the Brain-Voyager Brain Tutor (http://www.brainvoyager.com). Specifically, for each clearly identifiable major gyrus/sulcus, a certain number (ranging from 3–20) of landmarks were selected at cortical surface mesh vertices that are roughly distributed evenly along the gyral ridge/sulcal valley [36] and are sufficiently dense to ensure the full coverage of the whole gyral ridge/sulcal valley. In total, we interactively labeled 594 corresponding landmarks that fully cover the whole major gyral ridge/sulcal valley for each of the ten model brains. It should be noted that the number of initialized landmarks that fully cover the whole major gyral ridge/sulcal valley (here 594) does not affect the following group-wise landmark optimization result, since redundant landmarks are automatically merged during the optimization procedure (detailed in Section III-C). It should also be noted that our aim was not to accurately locate the anatomical correspondence of each landmark due to the highly variability of cortical folding patterns even within the same gyrus/sulcus across different subjects. We just enforced the roughly macroanatomical (gyri/sulci scale) correspondence for the landmarks to improve the accuracy of landmark initialization compared to the previous DICCCOL system and further to preserve the same anatomical identity of roughly corresponding landmarks during landmark optimization. Fig. 3(a) and (b) shows the brain template with labeled major gyri/sulci and the initialized

landmarks on gyri/sulci of one model brain, respectively. Fig. 3(c) shows all initialized 594 corresponding landmarks of three example model brains. These landmarks with rough anatomical correspondences served as the initial locations for group-wise optimization in the next step.

B. Structural Connection Pattern Homogeneity

Our prior studies [14], [18], [24] have demonstrated that the structural connection profile of an ROI could be highly nonlinear, that is, a slight change to the location, size, or shape of the ROI could significantly alter its DTI-derived fiber connection patterns. Therefore, this high nonlinearity could cause uncertainties and instabilities in the discovery of consistent and reproducible connectional landmarks. In this paper, we systematically examined the DTI-derived fiber structural connection pattern linearity/homogeneity of the cortical surface in detail.

Specifically, first, for each cortical mesh vertex, we extracted the DTI-derived white matter fiber bundles emanating from it to represent its structural connection pattern. Second, we used our recently developed trace-map model [18], [37] to quantitatively represent the fiber bundles. To be self-contained, the trace-map model projects a fiber bundle into a point distribution pattern on the standard surface of a unit sphere. One hundred forty four sample points are then set up on the standard sphere surface, and the point density of each sample point is calculated. Thus, a trace map is represented as a 144-dimension histogram vector, and each dimension is the point density information of a specific sample point. In this way, the problem of quantitatively comparing the similarities of fiber bundles is effectively converted to comparing the similarities of 144-dimension trace-map vectors [18], [37]. The major advantage of the trace-map model is its capability of accurately and compactly modeling global fiber shape patterns, while allowing for normal local shape variations [18], [37]. Third, for each cortical mesh vertex, we defined its structural connection pattern homogeneity as the similarity between its trace map and the trace maps of its morphological neighboring vertices (3-ring cortical surface mesh, i.e., about 30 vertices). Specifically, the similarity is calculated by the Kendall's coefficient of concordance [38]. Assume that k_i^j is the location of vertex j in subject i, and $tr\left(k_i^j\right)$ is the 144-dimension trace map of k_i^j. Assume that there are Q vertices in the neighborhood of k_i^j, and they are regarded as the object q to be ranked. Each of 144 dimensions of trace map is considered as a judge p [38], and the number of judges is denoted by P (P = 144). Define object q is given the rank $r_{q,p}$ by judge p, and t_k is the number of tied ranks in kth of m groups of ties. The Kendall's coefficient of concordance of k_i^j is defined as

$$W\left(k_i^j\right)=\frac{12\sum_{q=1}^{Q}\left(\sum_{p=1}^{p}r_{q,p}\right)^2-3P^2Q(Q+1)^2}{P^2\left(Q^3-Q\right)-P\sum_{k=1}^{m}\left(t_k^3-t_k\right)}. \quad (1)$$

The higher the Kendall's coefficient of concordance value, the more homogeneous the structural connection pattern of the vertex.

We calculated the structural connection pattern homogeneity values by (1) for all vertices of ten model brains. As shown in Fig. 4(c) and (d), we can see that there are vertices (highlighted by red bubbles) with local maximum of structural connection pattern homogeneity within the roughly corresponding cortical regions across different subjects. Moreover, we defined the distance of trace maps [21] as

$$D\left(tr, tr'\right) = \frac{\sum_{i=1}^{N}\left(tr_i - tr_i'\right)^2}{N} \quad (2)$$

where tr and tr' are two 144-dimension trace maps, tr_i and tr_i' are ith elements of tr and tr', and N is the number of trace-map dimensions ($N = 144$). We found that the structural connection patterns among the vertices with local maximum of structural connection pattern homogeneity (red bubbles) across the ten model brains have less trace-map distance, i.e., are more similar than those among the vertices in the morphological neighborhood (e.g., in the 1-ring, 3-ring, and 5-ring surface mesh neighborhood, highlighted by yellow, green, and purple bubbles, respectively, in Fig. 4(c) and (d) of the vertices with local maximum of structural connection pattern homogeneity. More results are in Supplemental Figs. 1 and 2. These results suggest that there are local structural connection pattern homogeneity peaks within the specific roughly corresponding cortical regions across different subjects, and importantly, these peaks exhibit more similar structural connection patterns compared to their morphological neighborhood. As illustrated previously, the high nonhomogeneity of structural connection profile of a ROI could cause uncertainties and instabilities in the discovery of consistent connectional landmarks [14], [18], [24]. Therefore, in this paper, we assumed that the identified corresponding connectional landmarks should tend to locate at the structural connection pattern homogeneity peaks in its local morphological neighborhood for all subjects. Our premise is that those corresponding connectional landmarks which locate at the structural connection pattern homogeneity peaks tend to have less nonhomogeneity and more reproducibility, in that the cortical regions on which they locate have more homogeneous and stable fiber connection patterns, as well as intersubject correspondences. We will integrate the structural connection pattern homogeneity information, which was not considered in our previous DICCCOL system, into our A-DICCCOL landmark optimization procedure which will be detailed in the following section.

C. Landmark Optimization

With the availability of initialized cortical landmarks in Section III-A, the next step of landmark identification is to perform landmark optimization by searching all possible combinations of candidate landmark locations within their local morphological neighborhoods in different model brains and seeking the optimal solution with the specific constraints. In our previous DICCCOL system, we only considered the DTI-derived fiber connection pattern similarity, which was defined as the distance of 144-dimension trace maps [21], as the constraint during landmark optimization to seek the optimal solution of group-wise fiber connection pattern consistency. In this paper, we substantially improved the landmark optimization procedure by adding three new meaningful constraints. First, the

corresponding landmarks across different model brains should locate on the same clearly identifiable gyrus/sulcus before and after optimization in order to preserve the same macroanatomical identity, as discussed in Section III-A. Second, the corresponding landmarks should tend to locate at the vertices with local maximum of structural connection pattern homogeneity within the morphological neighborhood, as discussed in Section III-B. Third, the landmark should move within the morphological neighborhood of its initial location with a predefined size during optimization to preserve the globally spatial correspondence on the cortical surface [16]. These three new constraints/information, as well as the DTI-derived fiber connection pattern similarity constraint adopted in previous DICCCOL system [21], were jointly modeled and integrated together to perform landmark optimization. The goal is to search all possible combinations of candidate landmark locations within their local morphological neighborhoods in different model brains and to seek the optimal solution of minimizing the group-wise variance of these four jointly modeled profiles.

Specifically, assume that there are M model brains, $\tilde{k}_i^j$ is the initialized location (mesh vertex) of landmark j in brain i, and k_i^j is the candidate location in its morphological neighborhood $C_{\tilde{k}_i^j}(\tilde{k}_i^j \in C_{\tilde{k}_i^j}$. The maximum principal curvature of k_i^j is represented by $p_{k_i^j}\begin{cases} \geq 0, & j \in \text{gyrus} \\ <0, & j \in \text{sulcus} \end{cases}$ [13] and it is used as the anatomical constraint.

First, $E_S(j)$ is defined as the structural connection pattern similarity constraint to ensure that the corresponding landmark j across M model brains have similar structural connection pattern, which was also adopted in our previous DICCCOL system [21]

$$E_S(j) = \text{var}\left(tr\left(k_1^j\right), tr\left(k_2^j\right), \ldots, tr\left(k_i^j\right)\right) \quad p_{k_i^j}\begin{cases} \geq 0, & j \in \text{gyrus} \\ <0, & j \in \text{sulcus} \end{cases} \tag{3}$$

where $tr\left(k_i^j\right)$ is the 144-dimension vector representing the trace map of k_i^j as detailed in Section II-D. var(·)is the variance among all trace-map vectors.

Second, $E_H(j)$ is defined as the structural connection pattern homogeneity constraint to ensure that the corresponding landmark j across M model brains should tend to move toward the location with local maximum of structural connection pattern homogeneity within its morphological neighborhood $C_{\tilde{k}_i^j}$ as detailed in Section III-B. After calculating the Kendall's coefficient of concordance Wk_i^j for k_i^j based on (1),

$$E_H(j) = \sum_{i=1}^{M}\left(1 - W\left(k_i^j\right)\right), p_{k_i^j}\begin{cases} \geq 0, & j \in \text{gyrus} \\ <0, & j \in \text{sulcus.} \end{cases} \tag{4}$$

Third, $E_D(j)$ is defined as the landmark spatial constraint to ensure that the landmark j moves within $C_{\tilde{k}_i^j}$ during the optimization procedure to preserve the globally spatial correspondence on the cortical surface, which is similar to the spatial constraints used in our recent work [16].

$$E_D(j) = \sum_{i=1}^{M} dist\left(k_i^j, \tilde{k}_i^j\right), \quad p_{k_i^j} \begin{cases} \leq 0, & j \in gyrus \\ <0, & j \in sulcus \end{cases} \tag{5}$$

where $dist(\cdot)$ is the Euclidean distance between k_i^j and $\tilde{k}_i^j$.

Mathematically, the group-wise variance of these four jointly modeled profiles is modeled as the energy E that we aim to minimize as follows based on (3)–(5):

$$E(j) = \lambda_1 E_S(j) + \lambda_2 E_H(j) + \lambda_3 E_D(j)$$
$$p_{k_i^j} \begin{cases} \geq 0, & j \in \text{gyrus} \\ <0, & j \in \text{sulcus}. \end{cases} \tag{6}$$

Here, we have weights $\lambda_1 + \lambda_2 + \lambda_3 = 1$ (λ_1,λ_2, and λ_3 are between 0 and 1). Note that we adopted the grid search and tenfold cross validation on ten model brains to find the optimal set of weights λ_1,λ_2, and λ_3 which have the least trace-map variance defined in (3) across ten model brains for each landmark. Then, we searched all possible combinations of candidate landmark locations k_i^j within their local morphological neighborhoods $C_{\tilde{k}_i^j}$ to seek the optimal solution of minimizing $E(j)$.

The energy $E(j)$ minimization was solved as follows. For each iteration, by searching the whole-space of landmarks candidate locations k_i^j in different model brains for one corresponding landmark j, we could find an optimal combination of landmark locations that minimized $E(j)$. The convergence criterion is that the Euclidean distance of landmark locations between two consecutive iterations is less than or equal to ε (ε = 2 mm, since the Euclidean distance between two adjacent surface mesh vertices is about 2 mm). Notably, for each iteration, if the distance between two neighboring landmarks that are to be optimized is less than or equal to a predefined threshold t_d (t_d = 2 mm, since the distance between two adjacent surface mesh vertices is about 2 mm) across all model brains, we labeled these two landmarks as “merged,” randomly discarded one of them in all model brains and only optimized the left one in the next iteration. In our implementation, we considered about 30 candidate locations (3-ring neighborhood) for each initialized landmark. The whole algorithm is summarized below.

Algorithm I

Landmark Optimization.

1: Initialization: $\tilde{k}^j_{0i}$ is the manually initialized location of landmark j in subject i, iteration number $t = 0$.

2: $argmin_{k_i^j} E(j), k_i^j \in C_{\tilde{k}^j_{0i}}$

3: $t = t + 1, \tilde{k}^j_{t_i} = k_i^j$

4: $argmin_{k_i^j} E(j), k_i^j \in C_{\tilde{k}^j_{ti}}$

5: If $\|\tilde{k}^j_{t_i} - \tilde{k}^j_{t-1_i}\| > \varepsilon$

6: repeat 3,4

7: end

D. Landmark Determination and Prediction

To examine and ensure the reproducibility of the identified cortical landmarks, we randomly divided the ten model brains equally into two groups and performed landmark optimization in Section III-C separately. As a result, two independent groups of optimized corresponding connectional landmarks were obtained. Then, for each optimized corresponding landmark in all of the ten model brains in two groups, we evaluated its consistency using both quantitative (trace-map distance and fiber connection pattern homogeneity values) and qualitative (visual inspection) methods similar as in [21] and [16]. In brief, for each corresponding landmark, we calculated the trace-map distance defined in (2) between any of the two brains within each of the two groups, and the mean trace-map distance of two groups were assessed to verify the similarity of the landmark across groups of brains [21]. We also assessed the average fiber connection pattern homogeneity values of the landmark in all model brains to verify if it increased after optimization. Meanwhile, we used in-house large-scale visualization tool [19] to visually confirm that the landmark preserved the same anatomical identity after optimization across all model brains. We also checked the fiber connection patterns in all model brains of two groups. If the landmark in any of the ten model brains has substantially different fiber shape patterns than others according to [21] and [16] based on quantitative (trace-map distance and fiber connection pattern homogeneity values) or qualitative (visual inspection) measurements, this landmark is discarded. Finally, we retained 555 connectional landmarks which exhibit reasonably accurate anatomical and connectional consistency across all ten model brains and named these 555 landmarks as A-DICCCOL. The visualizations of all 555 A-DICCCOL landmarks have been released online at http://dicccol.cs.uga.edu.

With the identified 555 A-DICCCOL landmarks, we were motivated to predict all 555 landmarks in a single subject's brain to verify the reproducibility and predictability of the A-DICCCOL landmarks. The prediction of A-DICCCOL landmarks in a testing brain was similar as the landmark optimization procedure in the Section III-C. First, the testing brain

was linearly registered to the same space of the model brains via FSL FLIRT, and thus, the A-DICCCOL landmarks in one of the model brains were roughly initialized in the testing brain. Second, the landmark optimization procedure in Section III-C was applied to the testing brain based on the optimized A-DICCCOL landmark locations in ten model brains. Since we already had the optimized locations of 555 A-DICCCOL landmarks in the ten model brains, we kept those optimized landmark locations in all model brains unchanged and only optimized those in the testing brain by minimizing the energy E defined in (6) across 11 brains (ten model brains and the testing brain). Thus, the landmark prediction procedure is fast and efficient. Specifically, assume m_1, m_2, …, m_{10} are the ten model brains and m_n is a testing brain, respectively. The landmark prediction algorithm is summarized below. It is clear that even though the performance of the prediction algorithm is dependent on the number of candidate locations in $C_{\tilde{k}^j_{0_n}}$ of m_n, it can be finished within linear time since the locations of A-DICCCOL landmarks of ten model subjects are unchanged. In practice, predicting all 555 A-DICCCOL landmarks in a testing brain takes around 30 min on a conventional computer at current stage.

Algorithm II

Landmark Prediction.

1: m_n is linearly registered to m_1 and 555 landmarks in m_1 are roughly initialized in m_n. $\tilde{k}^j_{0_n}$ is the initial location of landmark j in m_n.

2: Construct the new group, including m_1, m_2, …, m_{10} and m_n. Keep $\tilde{k}^j_{01}$, $\tilde{k}^j_{02}$, … $\tilde{k}^j_{010}$, be unchanged.

3: $argmin_{k^j_n} E(j)$, $k^j_n \in C_{\tilde{k}^j_{0_n}}$

4: k^j_n with least $E(j)$ is the predicted location of landmark j in m_n.

IV. RESULTS

The results section includes four sections as follows. Section IV-A demonstrates the reproducibility and predictability of the 555 A-DICCCOL landmarks. Section IV-B validates the consistency and stability of 555 landmarks based on HARDI data and using different fiber tracking software tools. Section IV-C focuses on the functional annotations of A-DICCCOL landmarks via T-fMRI data. Section IV-D compares the functional annotation accuracies by 555 A-DICCCOL landmarks and by image registration algorithms.

A. Reproducibility and Predictability of A-DICCCOL

We optimized and determined 555 consistent and corresponding A-DICCCOL landmarks in ten model brains as detailed in Section III-C and III-D and further predicted 555 landmarks in all testing brains in Datasets #1–#4 (see Table I) with DTI data (including the publicly released large-scale HCP high-quality DTI data (Q1 release) in Dataset #4) to examine the reproducibility and predictability of 555 A-DICCCOL landmarks. Fig. 5(a) shows the optimized 555 A-DICCCOL landmarks (yellow bubbles) in three model brains. As an

example, three of 555 landmarks are randomly selected (highlighted by three enlarged color bubbles, respectively) for all model brains to examine their anatomical, structural connection pattern similarity, and homogeneity consistency across different subjects in detail. First, Fig. 5(b) shows the DTI-derived fiber connection patterns of the three example landmarks across the three model brains in Fig. 5(a). By visual inspection, the fiber connection patterns of the same landmark across three model brains are similar. Quantitatively, the average trace-map distance calculated by (2) is 2.08, 2.18, and 2.15 within and across two groups of all ten model brains, respectively, which are considered as quite low [18], [21]. Moreover, the consistency of fiber structural connection pattern of corresponding landmarks across different subjects is significantly improved and shows group-wise consistency after landmark optimization than that of initialization, as illustrated in Fig. 6. To illustrate the effectiveness of fiber connection patterns, we also performed cortical registration via FreeSurfer based on the initialized locations of 555 A-DICCCOL landmarks on the ten model brains. In this way, we obtained a new set of 555 landmarks for each brain. Then, for each pair of corresponding landmarks based on cortical registration and the A-DICCCOL system, we calculated the Euclidean distance between the two landmarks. On average, the distance of all 555 landmarks across ten model brains is 1.54 mm, indicating that the 555 A-DICCCOL landmark locations indeed moved after adding meaningful fiber connection patterns constraints than merely anatomical constraints to improve the fiber connection correspondence. Second, in Fig. 5(c), the cortical surfaces are color-coded by structural connection pattern homogeneity values as illustrated in Section III-B. We can see that after landmark optimization, the three landmarks all converged to the locations (highlighted by the colored bubbles, respectively) with higher structural connection pattern homogeneity values than that of their initial locations (white bubbles), respectively. Supplemental Fig. 3 shows the mean structural connection pattern homogeneity values of all 555 landmarks in all ten model brains before and after optimization. We can see that mean homogeneity value increases after landmark optimization. Third, in Fig. 5(d), the cortical surfaces are color-coded by the maximum principal curvature value to indicate the gyri/sulci identity [13]. We can see that after optimization, the locations of three landmarks all maintained the same anatomical profiles as their initial locations, respectively. Finally, all of the 555 A-DICCCOL landmarks were evaluated and confirmed to possess the anatomical, structural connection pattern consistency across all model brains. The visualizations of structural connection patterns of all 555 A-DICCCOL landmarks have been released online at http://dicccol.cs.uga.edu.

Moreover, Fig. 5(h) shows the predicted 555 A-DICCCOL landmarks (yellow bubbles) in randomly selected three testing brains. The same three of 555 landmarks as in model brains [see Fig. 5(a)] are also selected (highlighted by the same three enlarged color bubbles, respectively) for the testing brains to examine their anatomical, structural connection pattern similarity, and homogeneity consistency across model brains and testing brains in detail. First, Fig. 5(e) shows the DTI-derived fiber connection patterns of the same three landmarks across the three testing brains in Fig. 5(h). By visual inspection, the fiber connection patterns of the same landmark across three testing brains [see Fig. 5(e)] as well as three model brains [Fig. 5(b)] are similar. Quantitatively, the average trace-map distance calculated by (2) is 2.14 within the three testing brains, which is similar as those in model brains and are

considered as quite low [18], [21]. Second, in Fig. 5(f), the cortical surfaces are color-coded by structural connection pattern homogeneity values. We can see that the predicted three landmarks are all at the locations (highlighted by the colored bubbles, respectively) with high structural connection pattern homogeneity values in its morphological neighborhood, respectively. Note that the initial locations (white bubbles) of landmarks in model brains [see Fig. 5(c)] which are used to illustrate the effectiveness of our landmark optimization procedure are not shown in the testing brains in Fig. 5(f). Third, in Fig. 5(g), the cortical surfaces are color-coded by the maximum principal curvature value to indicate the gyri/sulci identity [13]. We can see that the locations of three predicted landmarks all maintained the same anatomical profiles as those in model brains [Fig. 5(d)], respectively. Note that the initial locations (white bubbles) of landmarks in model brains [see Fig. 5(d)] which are used to illustrate the effectiveness of our landmark optimization procedure are not shown in the testing brains in Fig. 5(g). Moreover, Fig. 7 shows the fiber structural connection patterns of two examples of 555 A-DICCCOL landmarks in both model brains and testing brains of Datasets #1–#4 (see Table I) (including the publicly released large-scale HCP high-quality DTI data (Q1 release) in Dataset #4), respectively. We can see that the predicted A-DICCCOL landmarks possess structural connection pattern consistency across model brains and different testing brains including the publicly released HCP high-quality DTI data (Q1 release). More examples are in Supplemental Fig. 4. Finally, all of the 555 predicted A-DICCCOL landmarks were evaluated and confirmed to possess the structural connection pattern consistency across all model brains and about 120 testing brains (see Section II) including the publicly released HCP high-quality DTI data (Q1 release), indicating that the A-DICCCOL system is reproducible, predictable, and reasonably represents common cortical architectures with anatomical and structural connection pattern consistency across different subjects and populations.

B. Consistency of Landmarks in HARDI Data and Using Different Fiber Tracking Software Tools

In this section, we examined the consistency of 555 DTI-derived A-DICCCOL landmarks in HARDI data (Dataset #5 in Table I) because of its superior quality and capability of dealing with crossing fibers [39]. Moreover, since our A-DICCCOL landmarks identification depends on fiber structural connection patterns which might be affected by different fiber tracking strategies and software tools, we adopted five different fiber tracking software toolkits or parameter settings which more adequately account for crossing fibers [34] on HARDI data to examine the consistency of the 555 A-DICCCOL landmarks. Note that these validations were not considered in our previous DICCCOL system [21]. Specifically, first, we initialized 555 optimized A-DICCCOL connectional landmarks on all five brains with HARDI data by linear registration (FSL FLIRT). Second, five different fiber tracking software toolkits or parameter settings (including MRtrix [40] with three parameter settings (fiber bundle number is 10 000, 50 000, and 100 000, respectively), MEDINRIA based on q-ball imaging, and DTIStudio) were adopted to perform streamline fiber tracking on the HARDI data, respectively. Third, the landmark optimization procedure in Section III-C was applied to the five brains based on different fiber tracking software tools, respectively. Fig. 8 shows the covisualization of 555 optimized landmarks based on DTI/HARDI data and using different fiber tracking software tools, respectively. Quantitatively, we mapped all 555

landmarks in ten model brains and five HARDI brains using different fiber tracking software tools to the same space via linear transformation and calculated the mean distance of any pair of locations for each corresponding landmark. The overall mean distance for all landmarks is 4.37 mm, which is relatively small. In conclusion, the 555 A-DICCCOL landmarks are reasonably stable and consistent across subjects using DTI/HARDI data and different fiber tracking software tools.

C. Functional Annotations of A-DICCCOL

Similarly as in [21], the major objective of performing functional annotations of A-DICCCOL landmarks in this section is to demonstrate that A-DICCCOL landmarks with reasonably consistent anatomical, fiber structural connection pattern similarity, and homogeneity consistency also possess corresponding functional localizations. Specifically, first, similar to those in [18], [21], and [24], both group-level and individual-level fMRI activation peaks were detected by the traditional and well-established general linear model (GLM) via FSL FEAT and selected based on the five different task fMRI datasets in Section II (working memory, emotion, fear, semantic decision making, and empathy). Second, the group-level activation peaks were transformed back to each individual subject's space using the transformations derived from structural registrations via the FSL FLIRT [35]. The activation peaks that existed in both the group-wise map and individual map (defined if the distances between closest peaks are less than 8 mm) and were generated by the traditional and well-established GLM method can be used as the benchmark functional locations for each of brain activation maps [21]. Supplemental Fig. 5 shows one example of the group-level and individual-level fMRI activation peaks derived from the working memory task-based functional activation maps. In total, we identified 46 functional activation peaks from the five task-based functional activation maps. Third, as the 555 A-DICCCOL landmarks were identified in the DTI image space, all fMRI-derived functional peaks were mapped to the DTI space using the transformations derived from corresponding fMRI to DTI image registrations via the FSL FLIRT [24], [35]. Finally, we mapped each corresponding fMRI-derived functional peak to 555 A-DICCCOL maps via similar methods in [21]. More details are in supplemental materials. It is interesting that 46 A-DICCCOL landmarks were annotated and consistently colocalized in one or more 46 identified functional activation peaks across different subjects and/or populations as shown in Fig. 9. To quantitatively evaluate the functional annotation accuracy of the A-DICCCOLs, we measured the Euclidean distance between each annotated A-DICCCOL landmark and corresponding functional activation peak and reported the results in Fig. 9. Figs. 9(a) and (e) represents the results for semantic decision making [see Fig. 9(a)], emotion [see Fig. 9(b)], empathy [see Fig. 9(c)], fear [see Fig. 9(d)], and working memory [see Fig. 9(e)] activation map, respectively. In each figure, the functional activation peaks are highlighted by white bubbles, while the corresponding annotated A-DICCCOL landmarks are highlighted in other colors. The mean distance and standard deviation between each pair of functional peak and annotated landmark are shown in the histogram. The mean distances for the five functional activation maps are 6.27, 5.68, 6.38, 5.91, and 6.33 mm, respectively. Fig. 9(f) shows all of the functionally annotated A-DICCCOL landmarks, and the mean distance and standard deviation of each activation map are illustrated in the histogram. On average, the distance is 6.11 mm. The distances of each pair of functional activation peak and annotated A-

DICCCOL landmark in all subjects are shown in Supplemental Fig. 6. Furthermore, we measured the functional annotation accuracy of the same identified functional activation peaks by our previous DICCCOL [21] to have a comparison with A-DICCCOL. Specifically, for previous DICCCOL, the mean distances for the five task fMRI datasets are 6.50, 6.12, 5.93, 6.25, and 6.41 mm, respectively. On average, the distance is 6.24 mm. We can see that A-DICCCOL has higher functional annotation accuracy than previous DICCCOL. Moreover, we compared the mean distance of each functional activation peak of all five functional activation maps with the corresponding annotated A-DICCCOL landmark before and after optimization and generated by a random perturbation. The results are 6.78, 6.11, and 7.12 mm, respectively, indicating that in general, our optimized A-DICCCOL landmarks have better functional annotation accuracy than the landmarks before optimization or generated by a random perturbation. In conclusion, for each of the annotated 46 A-DICCCOL landmarks, it is reasonably consistently colocalized with a specific functional activation peak across most of the subjects, indicating that the A-DICCCOL system which has anatomical and structural connection pattern consistency also reasonably represents functional correspondences across different subjects and populations.

D. Comparisons With Image Registration Algorithms

We compared the functional annotation accuracies of functional activation peaks by our A-DICCCOL landmarks and with those by five representative different volumetric/surface registration algorithms. For volumetric registration, we adopted four algorithms including one linear (FSL FLIRT [35]) and three nonlinear ones (FSL FNIRT [41], ANTS [5], and HAMMER [3]). For surface-based registration, we used the FreeSurfer nonlinear algorithm [42]. The working memory functional activation map regions [see Fig. 9(e)] were used as the benchmark for comparisons here. Specifically, the A-DICCCOL annotation error is defined as the mean Euclidean distance between each pair of the annotated A-DICCCOL landmark and corresponding functional activation peak. The image registration based annotation error is defined as the mean Euclidean distance between the transformed fMRI activation peaks from individual brains to the MNI standard space via different registration methods and the centers of these multiple brains' transformed fMRI activation peaks. The detailed results are summarized in Supplemental Fig. 7. The average annotation errors in all subjects by the six methods (our A-DICCCOL landmarks, FLIRT, FNIRT, ANTS, HAMMER, and FreeSurfer) are 6.33, 7.76, 8.01, 7.74, 7.73 and 7.16 mm, respectively. The results show that our A-DICCCOL landmarks have higher functional annotation accuracy than these five image registration algorithms. It should be pointed out that the above compared image registration algorithms were designed for anatomical alignments, but not specifically for cortical landmark localization. If those image registration algorithms are optimized by taking the advantage of multimodal data in the future, their accuracies for landmark localization could be better than what was reported in this paper.

V. DISCUSSION AND CONCLUSION

In this paper, we presented a novel approach that identified 555 connectional cortical landmarks that turn out to be reproducible, predictable, and exhibit reasonably accurate anatomical, fiber connection pattern similarity, and homogeneity consistency across

individuals and populations. We initialized the connectional landmarks under anatomical guidance, added meaningful anatomical, structural connection pattern homogeneity, and spatial information into the following group-wise landmark optimization procedure, and applied the proposed connectional landmark discovery procedures on recently publicly released large-scale HCP high-quality DTI dataset, as well as HARDI data via different fiber tracking software tools to examine the consistency and stability of the DTI-derived connectional landmarks. Moreover, a portion of the connectional landmarks were functionally annotated by five functional activation maps derived from task fMRI datasets, demonstrating the reasonably functional correspondences of our connectional landmarks. We named these 555 connectional landmarks, which were generated by different and substantially improved strategies and procedures from our previous DICCCOL system [21], as anatomy-guided DICCCOL or A-DICCCOL. This A-DICCCOL system can be potentially used to report, integrate, transfer, and compare different measurements of the structural and functional properties of the brain, e.g., morphological measurements derived from structural MRI data and functional measurements derived from resting state fMRI data [20].

The presented A-DICCCOL system can be possibly further improved in the following directions in the future. First, we co-visualized A-DICCCOL and previous DICCCOL on the same brains and found that there are ten landmarks overlapped (Supplemental Fig. 8). Our interpretations are: 1) the A-DICCCOLs were interactively initialized along the gyral ridge/sulcal valley, while the initialization of previous DICCCOL was merely based on randomly sampled grid points and did not integrate rich anatomic information as we discussed in Section I in detail. In this way, the A-DICCCOL system can discover many landmarks on the gyral crowns and sulci fundi, which the previous DICCCOL initialization procedure based on linear registration could have possibly missed. 2) There are potentially previous DICC-COL landmarks located in the banks between gyral crowns and sulcal fundi that cannot be discovered by A-DICCCOL. Since the proposed A-DICCCOL system and our previous DICCCOL system use different discovery routines, the spatial localization difference between these two sets of landmarks is reasonable. In the future, we can potentially integrate parts of the strategies adopted in these two systems together to identify more consistent connectional landmarks. We believe that the identified 555 landmarks in A-DICCCOL are still a portion of all consistent landmarks across human brains. For example, the random initialization used in our previous DICCCOL system might be implemented prudentially to complement the interactive initialization in our A-DICCCOL system by considering landmark initialization positions in the banks in-between the gyral crowns and sulcal fundi. In this case, additional consistent connectional landmarks can be possibly discovered in cortical regions that A-DICCCOL has not considered. Moreover, there might potentially be more consistent cortical landmarks to be identified and discovered in the future, if we improve our discovery procedures in other aspects. For instance, an improvement we can possibly make is to integrate additional constraints into the optimization procedure, e.g., functional homogeneity [43], in the future.

Second, the functional annotations of A-DICCCOL landmarks are still far from being comprehensive and systematic. In this work, we used five T-fMRI datasets to explore the functional correspondences and annotations of a small portion of these 555 DTI-derived

consistent landmarks. Though the preliminary results are encouraging, in the future, more specific, large-scale task fMRI datasets should be designed and performed for the purpose of functional annotation of our A-DICCCOL landmarks, since the five T-fMRI datasets used in this paper were not aiming for functional annotation purpose initially, thus only annotated a small subset of all 555 A-DICCCOL landmarks. In addition, we can consider leveraging existing rich fMRI literature and existing databases such as the BrainMap data [44] to perform functional annotations of the discovered A-DICCCOL landmarks. As a result, the functional meanings of the A-DICCCOL landmarks can be then interpreted and applied in neuroscience applications. Once the anatomical, DTI-derived fiber structural connection pattern, and functional correspondences of the A-DICCCOL landmarks are established across individuals and populations, the A-DICCCOL system will offer a general platform to examine functional interaction [45] and dynamics [46] of the brain.

This paper has been focused on the presentation of methodologies and validation studies of the A-DICCCOL system, and the potential of its application in neuroscience and neuroimaging fields will be left to our future studies. For instances, the A-DICCCOL-based representation of large-scale reasonably common structural cortical architecture may provide opportunities for many basic science and clinical applications such as mapping human brain connectomes [21], [47]–[51] and elucidations of possible large-scale connectivity alterations in brain diseases [20], [52]–[55]. In short, the A-DICCCOL-based representation of reasonably common cortical architecture offers a principled approach and a generic platform to share, exchange, integrate, and compare multimodal neuroimaging datasets across laboratories, and we predict that public release of our A-DICCCOL system (http://dicccol.cs.uga.edu) will stimulate and enable various collaborative efforts in brain sciences, as well as contributing to data-driven discovery brain imaging studies. For instance, different labs and researchers can contribute their multimodal DTI and fMRI datasets to further perform functional annotations and validation of those A-DICCCOL landmarks in healthy brains and tailor them toward different brain disease populations (e.g., [20]), for the purpose of studying functions and dysfunctions of the human brain.

Supplementary Material

Refer to Web version on PubMed Central for supplementary material.

Acknowledgments

The authors would like to thank C. Faraco and L. S. Miller for sharing the working memory task design and the associated DTI/T-fMRI data.

The work of T. Liu was supported by the NSF CAREER Award (IIS-1149260), NIH R01 DA-033393, NIH R01 AG-042599, and NSF CBET-1302089. The work of L. Guo was supported by NSFC 61273362 and NSFC 61333017 and the work of T. Zhang and J. Lv was supported by the China Government Scholarship and the Doctorate Foundation of Northwestern Polytechnical University.

References

1. Thompson PM, Toga AW. A surface-based technique for 1336 warping 3-dimensional images of the brain. IEEE Trans Med Imag. Aug; 1996 15(4):1–16.

2. Fischl B, Salat DH, Busa E, Albert M. Whole brain segmentation: Automated labeling of neuroanatomical structures in the human brain. Neuron. 2002; 33(3):341–355. [PubMed: 11832223]
3. Shen D, Davatzikos C. HAMMER: hierarchical attribute matching mechanism for elastic registration. IEEE Trans Med Imag. Nov; 2002 21(11):1421–1439.
4. Van Essen DC, Dierker DL. Surface-based and probabilistic atlases of primate cerebral cortex. Neuron. 2007; 56(2):209–225. [PubMed: 17964241]
5. Avants BB, Epstein CL, Grossman M, Gee JC. Symmetric diffeomorphic image registration with cross-correlation: Evaluating automated labeling of elderly and neurodegenerative brain. Med Image Anal. 2008; 12:26–41. [PubMed: 17659998]
6. Jia H, Wu G, Wang Q, Shen D. ABSORB: Atlas building by self-organized registration and bundling. NeuroImage. 2010; 51(3):1057–1070. [PubMed: 20226255]
7. Yap P, Gilmore JH, Lin W, Shen D. POPTRACT: Population-based tractography. IEEE Trans Med Imag. Oct; 2011 30(10):1829–1840.
8. Zhang P, Cootes TF. Automatic part selection for groupwise registration. Inform Process Med Imag. 2011; 6801:85–96.
9. Asman AJ, Landman BA. Characterizing spatially varying performance to improve multi-atlas multi-label segmentation. Inform Process Med Imag. 2011; 6801:85–96.
10. Rettmann ME, Han X, Xu C, Prince JL. Automated sulcal segmentation using watersheds on the cortical surface. NeuroImage. 2002; 15(2):329–344. [PubMed: 11798269]
11. Behrens JBH, Robson TEJ, Drobnjak MD, Rushworth I, Brady MFS, Smith JM, Higham SM, Matthews DJ. Changes in connectivity profiles define functionally distinct regions in human medial frontal cortex. Proc Nat Acad Sci USA. 2004; 101:13335–13340. [PubMed: 15340158]
12. Jbabdi S, Woolrich MW, Behrens TEJ. Multiple-subjects connectivity-based parcellation using hierarchical dirichlet process mixture models. NeuroImage. 2009; 44:373–384. [PubMed: 18845262]
13. Li G, Guo L, Nie J, Liu T. Automatic cortical sulcal parcellation based on surface principal direction flow field tracking. NeuroImage. 2009; 46(4):923–937. [PubMed: 19328234]
14. Liu T. A few thoughts on brain ROIs. Brain Imag Behav. 2011; 5(3):189–202.
15. Poldrack RA. The future of fMRI in cognitive neuroscience. NeuroImage. 2011; 62:1216–1220. [PubMed: 21856431]
16. Li K, Guo L, Zhu D, Hu X, Han J, Liu T. Individual functional roi optimization via maximization of group-wise consistency of structural and functional profiles. Neuroinformatics. 2012; 10(3): 225–242. [PubMed: 22281931]
17. Zhang T, Guo L, Li K, Jing C, Hu X, Cui G, Li L, Liu T. Predicting functional cortical ROIs via DTI-derived fiber shape models. Cerebral Cortex. 2012; 22(4):854–864. [PubMed: 21705394]
18. Zhu D, Li K, Faraco C, Deng F, Zhang D, Jiang X, Chen H, Guo L, Miller S, Liu T. Discovering dense and consistent landmarks in the brain. Inform Process Med Imag. 2011; 22:97–110.
19. Li K, Guo L, Faraco C, Zhu D, Chen H, Yuan Y, Lv J, Deng F, Jiang X, Zhang T, Hu X, Zhang D, Miller LS, Liu T. Visual analytics of brain networks. NeuroImage. 2012; 61(1):82–97. [PubMed: 22414991]
20. Li K, Zhu D, Guo L, Li Z, Lynch ME, Coles C, Hu X, Liu T. Connectomics signatures of prenatal cocaine exposure affected adolescent brains. Human Brain Mapping. 2012; 34(10):2494–2510. [PubMed: 22461404]
21. Zhu D, Li K, Guo L, Jiang X, Zhang T, Zhang D, Chen H, Deng F, Faraco C, Jin C, Wee C, Yuan Y, Lv P, Yin Y, Hu X, Duan L, Hu X, Han J, Wang L, Shen D, Miller LS, Li L, Liu T. DIC-CCOL: Dense individualized and common connectivity-based cortical landmarks. Cerebral Cortex. 2013; 23(4):786–800. [PubMed: 22490548]
22. Saygin ZM, Osher DE, Koldewyn K, Reynolds G, Gabrieli JD, Saxe RR. Anatomical connectivity patterns predict face selectivity in the fusiform gyrus. Nat Neurosci. 2011; 15(2):321–327. [PubMed: 22197830]
23. Honey CJ, Sporns O, Cammoun L, Gigandet X, Thiran JP, Meuli R, Hagmann P. Predicting human resting-state functional connectivity from structural connectivity. Proc Nat Acad Sci USA. 2009; 106(6):2035–2040. [PubMed: 19188601]

24. Li K, Guo L, Faraco C, Zhu D, Deng D, Zhang T, Jiang X, Zhang D, Chen H, Hu H, Miller LS, Liu T. Individualized ROI optimization via maximization of group-wise consistency of structural and functional profiles. Adv Neural Inform Process Syst. 2010; 23:1369–1377.
25. Passingham RE, Stephan KE, Kotter R. The anatomical basis of functional localization in the cortex. Nature Rev Neurosci. 2002; 3(8):606–616. [PubMed: 12154362]
26. Uğurbil K, Xu J, Auerbach EJ, Moeller S, Vu AT, Duarte-Carvajalino JM, Lenglet C, Wu X, Schmitter S, Van de Moortele PF, Strupp J, Sapiro G, De Martino F, Wang D, Harel N, Garwood M, Chen L, Feinberg DA, Smith SM, Miller KL, Sotiropoulos SN, Jbabdi S, Andersson JL, Behrens TE, Glasser MF, Van Essen DC, Yacoub E, WU-Minn HCP Consortium. Pushing spatial and temporal resolution for functional and diffusion MRI in the human connectome project. Neuroimage. 2013; 80:80–104. [PubMed: 23702417]
27. Faraco CC, Unsworth N, Langley J, Terry D, Li K, Zhang D, Liu T, Miller LS. Complex span tasks and hippocampal recruitment during working memory. NeuroImage. 2011; 55(2):773–787. [PubMed: 21182968]
28. Sabatinelli D, Lang PJ, Bradley MM, Costa VD, Keil A. The timing of emotional discrimination in human amygdala and ventral visual cortex. J Neurosci. 2009; 29(47):14864–14868. [PubMed: 19940182]
29. Langleben DD, Loughead JW, Ruparel K, Hakun JG, Busch-Winokur S, Holloway MB, Strasser AA, Cappella JN, Lerman C. Reduced prefrontal and temporal processing and recall of high “sensation value” ads. NeuroImage. 2009; 46(1):219–225. [PubMed: 19457412]
30. Dennis NA, Browndyke JN, Stokes J, Need A, Burke JR, Welsh-Bohmer KA, Cabeza R. Temporal lobe functional activity and connectivity in young adult APOE 34 carriers. Alzheimer’s & Dementia. 2010; 6:303–311.
31. Nie J, Guo L, Li K, Wang Y, Chen G, Li L, Chen H, Deng F, Jiang X, Zhang T, Huang L, Faraco C, Zhang D, Guo C, Yap P, Hu X, Li G, Lv J, Yuan Y, Zhu D, Han J, Sabatinelli D, Zhao Q, Miller LS, Xu B, Shen P, Platt S, Shen D, Hu X, Liu T. Axonal fiber terminations concentrate on gyri. Cerebral Cortex. 2012; 22(12):2831–2839. [PubMed: 22190432]
32. Liu T, Li H, Wong K, Tarokh A, Guo L, Wong S. Brain tissue segmentation based on DTI data. NeuroImage. 2007; 38(1):114–123. [PubMed: 17804258]
33. Liu T, Nie J, Tarokh A, Guo L, Wong S. Reconstruction of central cortical surface from mri brain images: Method and application. NeuroImage. 2008; 40(3):991–1002. [PubMed: 18289879]
34. Fillard P, Descoteaux M, Goh A, Gouttard S, Jeurissen B, Malcolm J, Ramirez-Manzanares A, Reisert M, Sakaie K, Tensaouti F, Yo T, Mangin JF, Poupon C. Quantitative evaluation of 10 tractography algorithms on a realistic diffusion MR phantom. Neuroimage. 2011; 56(1):220–234. [PubMed: 21256221]
35. Jenkinson M, Smith SM. A global optimisation method for robust affine registration of brain images. Med Image Anal. 2001; 5(2):143–156. [PubMed: 11516708]
36. Deng F, Jiang X, Zhu D, Zhang T, Li K, Guo L, Liu T. A functional model of cortical gyri and sulci. Brain Struct Funct. 2014; 219:1473–1491. [PubMed: 23689502]
37. Zhu D, Li K, Faraco C, Deng F, Zhang D, Jiang X, Chen H, Guo L, Miller L, Liu T. Optimization of functional brain rois via maximization of consistency of structural connectivity profiles. NeuroImage. 2011; 59:1382–1393. [PubMed: 21875672]
38. Siegel, S., Castellan, NJ, Jr. Nonparametric Statistics for the Behavioral Sciences. 2nd. New York, NY, USA: McGraw-Hill; 1988. p. 266
39. Tuch DS, Reese TG, Wiegell MR, Makris N, Belliveau JW, Wedeen VJ. High angular resolution diffusion imaging reveals intravoxel white matter fiber heterogeneity. Magn Res Med. 2002; 48(4): 577–582.
40. Tournier JD, Calamante F, Connelly A. MRtrix: Diffusion tractography in crossing fiber regions. Int J Imag Syst Technol. 2012; 22(1):53–66.
41. Jenkinson M, Beckmann CF, Behrens TE, Woolrich MW, Smith SM. FSL. Neuro Image. 2012; 62:782–790. [PubMed: 21979382]
42. Fischl B, Sereno MI, Tootell RB, Dale AM. High-resolution intersubject averaging and a coordinate system for the cortical surface. Human Brain Mapping. 1999; 8:272–284. [PubMed: 10619420]

43. Craddock RC, James GA, Holtzheimer PE III, Hu XP, Mayberg HS. A whole brain fMRI atlas generated via spatially constrained spectral clustering. Human Brain Mapping. 2012; 33(8):1914–1928. [PubMed: 21769991]
44. Laird AR, Eickhoff SB, Kurth F, Fox PM, Uecker AM, Turner JA, Robinson JL, Lancaster JL, Fox PT. ALE meta-analysis workflows via the BrainMap database: Progress towards a probabilistic functional brain atlas. Neuroinformatics. 2009; 3:23.
45. Sun J, Hu X, Huang X, Liu Y, Li K, Li X, Han J, Guo L, Liu T, Zhang J. Inferring consistent functional interaction patterns from natural stimulus FMRI data. NeuroImage. 2012 in press.
46. Hu X, Guo L, Zhang D, Li K, Zhang T, Lv J, Han J, Liu T. Assessing the dynamics on functional brain networks using spectral graph theory. Proc Int Symp Biomed Imag. 2011:2144–2149.
47. Williams R. The human connectome: just another 'ome. Lancet Neurol. 2010; 9(3):238–239. [PubMed: 20170838]
48. Kennedy DN. Making connections in the connectome era. Neuroinformatics. 2010; 8(2):61–62. [PubMed: 20428970]
49. Biswal BB, Mennes M, Zuo XN, Gohel S, Kelly C, Smith SM, Beckmann CF, Adelstein JS, Buckner RL, Colcombe S, Dogonowski AM, Ernst M, Fair D, Hampson M, Hoptman MJ, Hyde JS, Kiviniemi VJ, Kötter R, Li SJ, Lin CP, Lowe MJ, Mackay C, Madden DJ, Madsen KH, Margulies DS, Mayberg HS, McMahon K, Monk CS, Mostofsky SH, Nagel BJ, Pekar JJ, Peltier SJ, Petersen SE, Riedl V, Rombouts SA, Rypma B, Schlaggar BL, Schmidt S, Seidler RD, Siegle GJ, Sorg C, Teng GJ, Veijola J, Villringer A, Walter M, Wang L, Weng XC, Whitfield-Gabrieli S, Williamson P, Windischberger C, Zang YF, Zhang HY, Castellanos FX, Milham MP. Toward discovery science of human brain function. Proc Nat Acad Sci United States Amer. 2010; 107(10): 4734–4739.
50. Van Dijk KR, Hedden T, Venkataraman A, Evans KC, Lazar SW, Buckner RL. Intrinsic functional connectivity as a tool for human connectomics: Theory, properties, and optimization. J Neurophysiol. 2010; 103(1):297–321. [PubMed: 19889849]
51. Hagmann P, Cammoun L, Gigandet X, Gerhard S, Grant PE, Wedeen V, Meuli R, Thiran JP, Honey CJ, Sporns O. MR connectomics: Principles and challenges. J Neurosci Methods. 2010; 194:34–45. [PubMed: 20096730]
52. Suvak MK, Barrett LF. Considering PTSD from the perspective of brain processes: A psychological construction approach. J Trauma Stress. 2011; 24(1):3–24. [PubMed: 21298725]
53. Dickerson BC, Sperling RA. Large-scale functional brain network abnormalities in Alzheimer's disease: Insights from functional neuroimaging. Behav Neurol. 2009; 21(1):63–75. [PubMed: 19847046]
54. Seeley WW, Crawford RK, Zhou J, Miller BL, Greicius MD. Neurodegenerative diseases target large-scale human brain networks. Neuron. 2009; 62(1):42–52. [PubMed: 19376066]
55. Supekar K, Menon V, Rubin D, Musen M, Greicius MD. Network analysis of intrinsic functional brain connectivity in Alzheimer's disease. PLoS Comput Biol. 2008; 4(6):e1000100. [PubMed: 18584043]

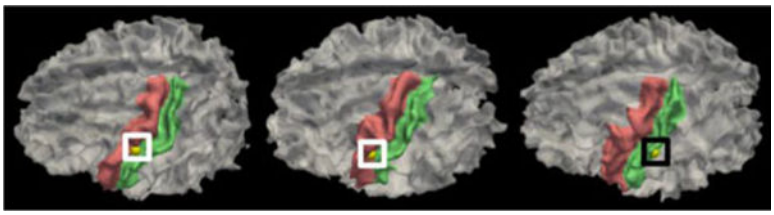

Fig. 1.

Initialization of a corresponding DICCCOL landmark located on the left precentral gyrus in three example brains via linear registration [21]. The landmark is highlighted by yellow bubble. The landmarks highlighted by the white boxes in first two brains are located in the left precentral gyrus (highlighted by red), while the landmark highlighted by the black box in third brain is located in the left postcentral gyrus (highlighted by green).

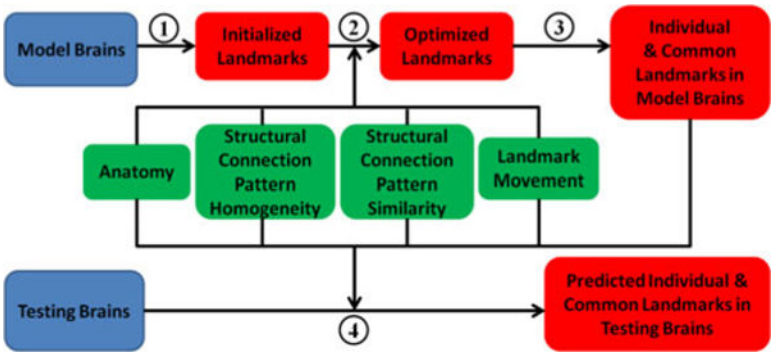

Fig. 2.

Flowchart of the computational framework for the A-DICCCOL landmark identification. Step 1: landmark initialization; Step 2: landmark optimization (four constraints are highlighted by the green boxes, respectively); Step 3: landmark determination; Step 4: landmark prediction.

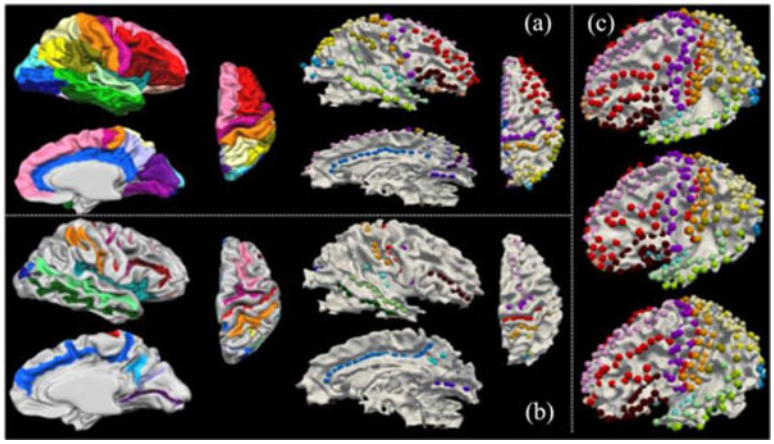

Fig. 3.

Visualization of initialized landmarks on the model brains. (a) The brain template with labeled major gyri, and the corresponding initialized landmarks of one example model brain. (b) The brain template with labeled sulci, and the corresponding initialized landmarks of the same model brain in (a). Note that the initialized landmarks on corresponding gyri/sulci in (a) and (b) are highlighted in the same color with the brain template. (c) All 594 initialized landmarks in three example model brains.

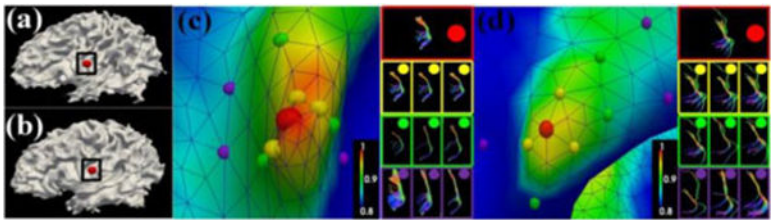

Fig. 4.

Illustration of structural connection pattern homogeneity. (a) and (b) Initialized landmark (highlighted by red bubbles) within roughly corresponding regions (highlighted by black boxes) in two model brains. (c) and (d) Zoomed views of the roughly corresponding regions within the black boxes in (a) and (b). Cortical regions are color-coded by structural connection pattern homogeneity values. The color bar is in the bottom right. The vertices with local maximum of homogeneity and other example vertices in the 1-ring, 3-ring and 5-ring neighborhood are shown in red, yellow, green, and purple bubbles, respectively. The fiber shape patterns of the vertices in the left panel are shown in the right panel.

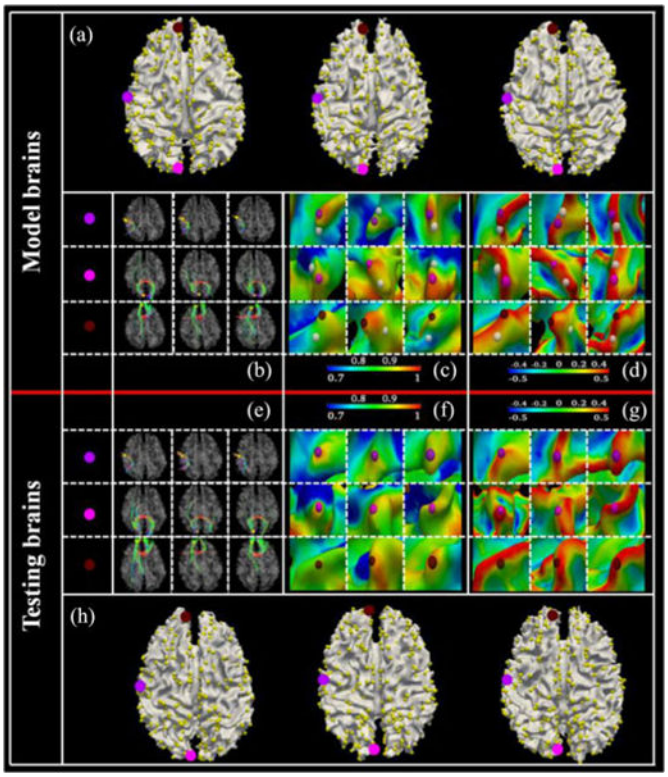

Fig. 5.

555 A-DICCCOL landmarks in model brains [see Fig. 5(a)–(d)] and testing brains [see Fig. 5(e)–(h)], respectively. (a) and (h) Optimized 555 landmarks in three model brains and three testing brains, respectively. Three example corresponding A-DICCCOL landmarks (highlighted by enlarged color bubbles) are selected for all model brains and testing brains. (b) and (e) DTI-derived fiber connection patterns of the three example landmarks across the three model brains and three testing brains, respectively. In each figure, each row represents a corresponding landmark in three model brains/testing brains. (c) Optimized locations (color bubbles) and initial locations (white bubbles) of the three landmarks on the three model brains' cortical surfaces which are color-coded by structural connection pattern homogeneity value. Each row represents a corresponding landmark in three model brains. The color bar is at the bottom. (d) Optimized locations (color bubbles) and initial locations (white bubbles) of the three landmarks on the three model brains' cortical surfaces which are color-coded by the maximal principal curvature value. Each row represents a corresponding landmark in three model brains. The color bar is at the bottom. (f) Predicted locations (color bubbles) of the three landmarks on the three testing brains' cortical surfaces which are color-coded by structural connection pattern homogeneity value. Each row represents a corresponding landmark in three testing brains. The color bar is at the top. (g) Predicted locations (color bubbles) of the three landmarks on the three testing brains' cortical surfaces which are color-coded by the maximal principal curvature value. Each row represents a corresponding landmark in three testing brains. The color bar is at the top.

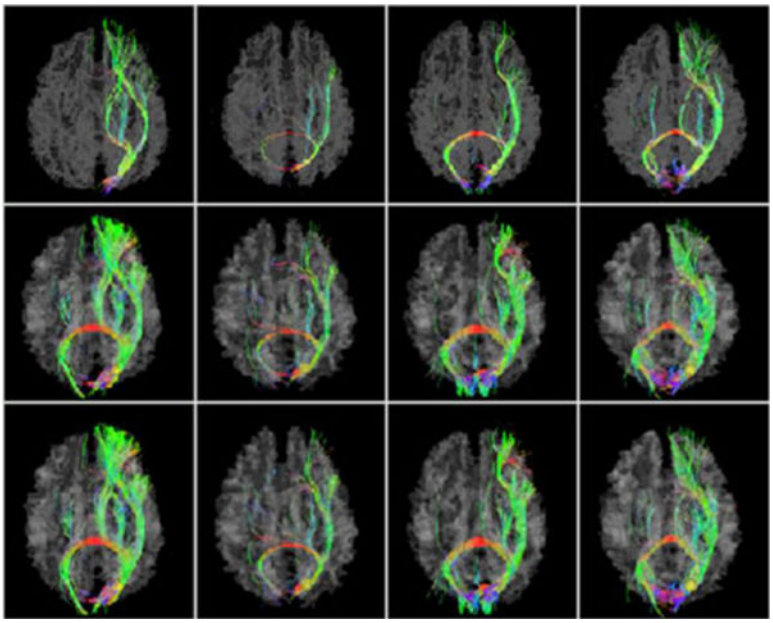

Fig. 6.

One example of 555 A-DICCCOL landmarks. Row 1–3 show the fiber structural connection patterns of the same landmark before optimization in four model brains, after optimization in four model brains, and in four testing brains, respectively. The landmarks are shown by the yellow bubbles.

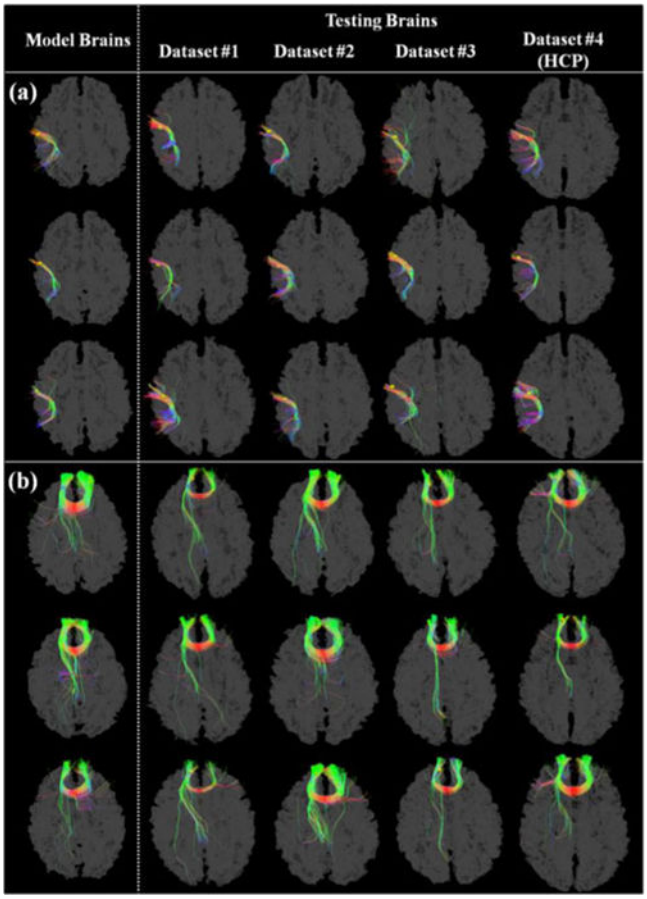

Fig. 7.

(a) and (b) Two examples of 555 A-DICCCOL landmarks in both model brains and testing brains of four different datasets (see Table I), respectively. Note that Dataset #4 is the publicly released large-scale HCP high-quality DTI data (Q1 release). In each figure, the first column shows the fiber structural connection patterns of the same corresponding landmark in three example model brains, respectively. The second to fifth rows are the fiber structural connection patterns of the same predicted A-DICCCOL landmark in three example testing brains of Datasets #1–#4 (see Table I), respectively. The landmarks are shown by the yellow bubbles.

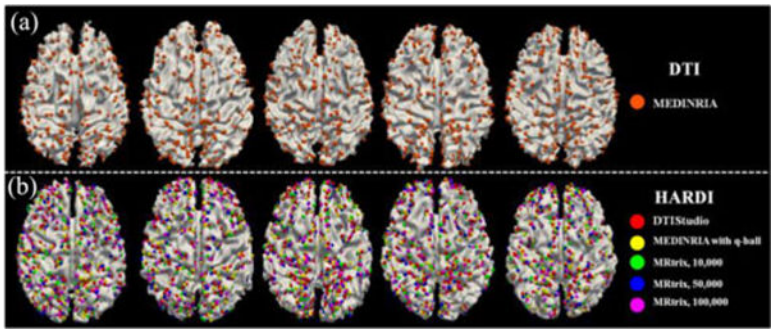

Fig. 8.

Covisualization of 555 optimized landmarks based on different fiber tracking software tools and using HARDI data, respectively. (a) 555 optimized landmarks (orange bubbles) on the five model brains based on DTI data and MEDINRIA software. (b) 555 optimized landmarks on the five HARDI brains using different fiber tracking software tools are highlighted by red, yellow, green, blue, and purple bubbles, respectively.

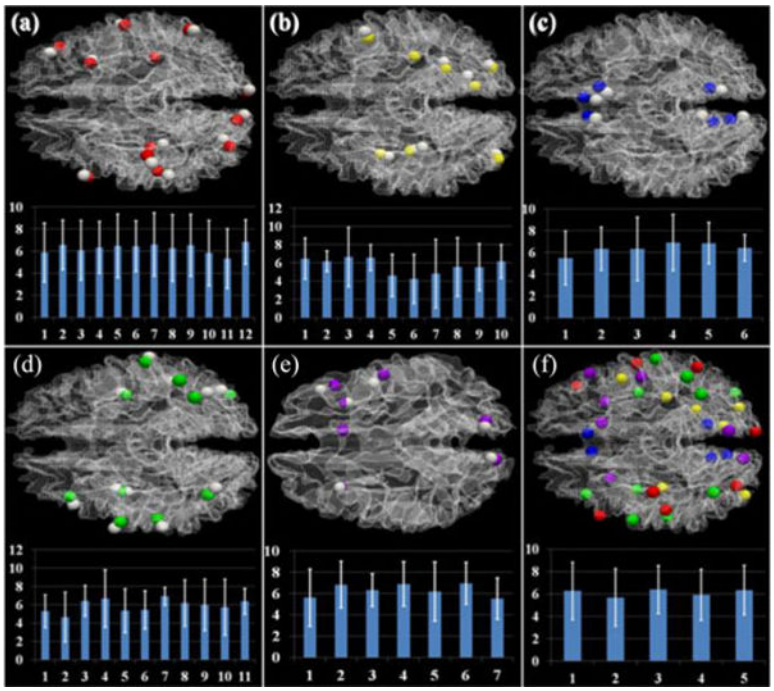

Fig. 9.

Functional annotations of A-DICCCOL landmarks based on 46 fMRI-derived functional activation peaks (a) and (e). (a) Semantic decision making, (b) emotion, (c) empathy, (d) fear, and (e) working memory activation map, respectively. In each figure, the functional activation peaks are highlighted by white bubbles, while the corresponding annotated A-DICCCOL landmarks are highlighted in other color bubbles. The mean distance and standard deviation between each pair of functional activation peak and annotated landmark are shown in the histogram in the bottom panel, in which the horizontal axis indexes activation peaks and the vertical axis represents the distance (mm). (f) All of the functionally annotated landmarks and the mean distance and standard deviation of each functional activation map.

TABLE I

SUMMARY OF FIVE DIFFERENT DATASETS

Datasets	No. of Subjects	Types	Functional Activation Maps	Model/Testing Brains
# 1	23	DTI, one T-fMRI scan	Working memory	10 out of 23: Model; the others: Testing
# 2	13	DTI, five T-fMRI scans	Emotion, empathy, fear, semantic decision making, working memory	Testing
# 3	20	DTI	None	Testing
# 4 (HCP)	68	DTI	None	Testing
# 5	5	HARDI	None	Testing